Three-dimensional sector-wise golden-angle (3D-SWIG) – Improved k-space uniformity after ECG binning compared to conventional 3D golden-angle profile ordering

Alexander Fyrdahl[1], Joao G Ramos[1], Martin Ugander[1,2], Andreas Sigfridsson[1]

[1] Department of Clinical Physiology, Karolinska University Hospital, and Karolinska Institutet
Stockholm, Sweden

[2] The Kolling Institute, Royal North Shore Hospital, and Northern Clinical School, Sydney Medical School, University of Sydney, Sydney, Australia

Correspondence to:

Andreas Sigfridsson, PhD

Department of Clinical Physiology, NKS C8:27

Karolinska University Hospital

SE-171 76 Stockholm

Sweden

andreas.sigfridsson@gmail.com

Abstract

Purpose. In this study, we propose a three-dimensional sector-wise golden-angle (3D-SWIG) profile ordering that preserves k-space uniformity after ECG binning.

Methods. A balanced SSFP pulse sequence was implemented with 3D-SWIG radial ordering, were the trajectory sphere was divided into sectors, and each heartbeat was acquired in a separate sector. The proposed method was evaluated both in phantom and *in vivo*. A phantom was scanned at 3T using the 3D-SWIG sequence and a conventional 3D golden-angle sequence. Acquisitions were performed with 12, 48 and 192 simulated heartbeats, i.e. sectors in the 3D-SWIG sequence. Three subjects were imaged with the same protocol, with 48 heart beats during free breathing. Physiological binning was performed and the uniformity was assessed through spherical Voronoi tessellation. Analysis of the point spread function was performed to estimate the amount of aliasing. Qualitative assessment was performed by visual assessment of M-mode images.

Results. In phantoms, 3D-SWIG showed fewer streaking artifacts from undersampling compared to conventional golden-angle. *In vivo,* the difference was further exacerbated as the conventional golden-angle profile ordering resulted in completely non-diagnostic images. Compared to golden-angle profile ordering, 3D-SWIG consistently had a lower standard deviation of the mean Voronoi cell area, indicating superior sampling uniformity, thus corroborating the qualitative results.

Conclusions: Conventional golden-angle imaging suffers from sampling heterogeneity after ECG binning. 3D-SWIG offers a simple solution which highly improves k-space uniformity even at high undersampling factors. This study demonstrates how 3D-SWIG can enable whole-heart cine imaging during free breathing with an acquisition time of less than one minute.

Introduction

In comparison to other uses of magnetic resonance imaging, cardiovascular magnetic resonance (CMR) stands out as particularly demanding with regards to the duration of acquisition. In addition to the time needed to prepare the patient, it is common to have to acquire one or several survey scans, followed by several planning projections, such as vertical and horizontal long axes and a pseudo-short-axis before being able to identify the standard projections of 2-, 3- and 4-chamber views as well as true short axis orientations used for clinical diagnosis. Advances have been made using automated slice planning (1,2) but this is only available on the very latest generations of scanners and has yet to see widespread adaptation. Furthermore, every CMR acquisition will typically require the patient to perform one or several breath holds, where every breath hold has to be initiated by a voice instruction and has to be followed by a recovery period of variable length in order for the patient to recover before the next breath hold. Patient compliance can be highly variable, and repeat acquisitions are not a rare occurrence. Even seemingly successful breath holds can lead to slice misalignment as it might be difficult for the patient to repeatedly hold their breath in the same position. The current practice is to use end-expiratory breath holds. Although they may be tougher to perform for some patients, they may improve repeatability in breath hold position and reduce slice misalignment in two-dimensional CMR (3). An alternate strategy is to get rid of breath held acquisitions all together. To this end, much work has been done towards enabling entirely free-breathing image acquisition strategies (4–6). In recent years, a number of studies have been published describing whole-heart free-breathing imaging, either by compensating for respiratory motion (7,8) or by resolving the respiratory motion as an extra time dimension (9–11). The aforementioned methods have all shown promising results, albeit with long acquisition times. This typically also entails long reconstruction times, up to several hours, which means that previous methods are not yet clinically feasible, or are at least impractical to adapt outside of research centers.

Another reason for repeat acquisitions may be imperfect planning of slice positions. A major benefit of acquiring the whole heart in a single volume is that decisions regarding slice planning are not final, and new slice orientations can be prescribed after the patient has left the scanner. This is especially useful in patients with congenital heart defects, where the slice prescription may be challenging. Many such methods are based on golden-angle radial techniques. While promising for real-time imaging, where successive readouts are used, golden-angle techniques have displayed poor compatibility with physiological binning. Physiological binning tends to leave gaps in the sampling pattern (12), which not only promotes streaking artifacts but also severely limits the use of higher undersampling factors. Recent work has introduced the PC-SWIG method (13) which enables 2D golden-angle radial phase contrast imaging with preserved k-space uniformity after binning by dividing the k-space into multiple radial sectors, were each heart beat is acquired in a separate sector. The preserved k-space uniformity means that images can be reconstructed at high temporal resolution, or that images with high image quality can be reconstructed from very little data. In this work, we propose to extend the 2D-SWIG method (13) to an analogous 3D-SWIG method based on acquiring a spherical k-space in spherical sectors, where each sector is acquired during a single heartbeat. In combination with projection based self-navigation (14) and rigid motion correction, we demonstrate the feasibility of whole-heart functional imaging in less than a minute.

Theory

The double golden-angle method (15) is based on two so-called golden means, which conventionally have been defined as $\phi_1 = 0.4656$ and $\phi_2 = 0.6823$ (16). The construction of a conventional double golden-angle profile ordering can be described in two stages. First, the sampling coordinates are mapped onto a two-dimensional unit square, with coordinates

determined by

$$x = \{m\phi_1\}, \quad y = \{m\phi_2\} \tag{1}$$

where m counts the readout number and $\{\}$ denotes the modulo of 1 (17). The unit square can then be mapped to the surface of a three-dimensional sphere or hemisphere to determine a radial readout starting point in k-space .To maintain the k-space uniformity, it's desired that the mapping from the plane to the sphere should fulfill some criteria, namely to be minimally distorting while simultaneously preserving the surface area. In previous 3D golden-angle implementations (15), the Lambert azimuthal equal-area projection has been shown effective. The spherical coordinates α and β, denoting the azimuthal and polar angles are found as

$$\alpha = 2\pi\{m\phi_2\}, \quad \beta = cos^{-1}(\{m\phi_1\}) \tag{2}$$

Analogous to the previously described 2D-SWIG method, the surface of the trajectory hemisphere can be divided in a nearly-uniform grid, and each heartbeat can be acquired with the starting points of the radial spokes within a unique grid cell. Each cell can be treated as a unit square, similar to the conventional double golden-angle method. By distributing the starting points within the unit square as described in Eq. (2), and mapping the unit square to the trajectory hemisphere, k-space sampling can be determined. We recall that the desired mapping from a plane to a sphere should preserve the fractional surface area and add minimal distortion to the distribution of sampling points. Many simplistic methods for determining spherical grids will result in severe distortions either at the poles or the equator. Instead, we propose a modified mapping from a half-cube to a hemisphere, defined by

$$X' = x \cdot \sqrt{1 - \frac{y^2}{2} - \frac{z^2}{2} - \frac{y^2 z^2}{3}} \tag{3}$$

$$Y' = y \cdot \sqrt{1 - \frac{z^2}{2} - \frac{z^2}{2} - \frac{z^2 y^2}{3}} \tag{4}$$

$$Z' = z \cdot \sqrt{1 - \frac{x^2}{2} - \frac{y^2}{2} - \frac{x^2 y^2}{3}} \tag{5}$$

where lower case variables x, y and z corresponds to coordinates on the cube whereas X', Y' and Z' corresponds to coordinates on the sphere, in a Cartesian coordinate system (18). The transform to spherical coordinates is trivial, and omitted for brevity. A schematic overview of the tiling is displayed in Figure 1.

Methods

Time expenditure

An experienced CMR radiographer was timed using a stop watch (iPhone, Apple Inc., Cupertino, CA) while prescribing slices and subsequently acquiring images for a standard of care CMR study. The timer was started after the initial survey scan was completed, as it would have been necessary to acquire regardless of the exam or strategy used. The time to acquire all initial planning slices was recorded. This included extra anatomical localizers at the radiographer's discretion, such as horizontal- or vertical long axes (HLA and VLA) as well as a pseudo short-axis. The recorded time also included the time needed for providing necessary instructions to the patient, such as instructing them about breath holds or reminding them to stay still between acquisitions. When all initial localizers were acquired, the time needed to plan the actual anatomical projections was recorded. This included 2-, 3- and 4-chambers as

well as a short-axis stack. This time also included the amount of time spent on placing the slice positions for all axes. Finally, the time to execute the acquisitions was calculated based on the time needed to play back the pre-recorded voice commands. The acquisition times for each sequence were calculated, assuming a regular heart rate of 60 beats/min and 12 contiguous slices needed to cover the left ventricle in the short-axis view. This was compared to the expected time to acquire the 3D-SWIG volume using an average heart rate of 60 beats/min and the time needed to find the anatomical projections from the 3D-stack.

Pulse sequence

A prototype 3D radial balanced steady state free precession (bSSFP) pulse sequence with a non-selective excitation pulse was modified in-house to accommodate the proposed 3D-SWIG profile ordering, and the extended triggering logic that modified the profile ordering based on feedback from the patient monitoring unit was added. A user interface parameter allowed the operator to select between 12, 48 or 192 segments. During runtime, a dummy heart beat was acquired to establish a signal steady-state, followed by 12, 48 or 192 heartbeats, each of which were acquired in a separate sector on the trajectory sphere surface. Trajectory coordinates were calculated using Eq. (3–5). The profile ordering included a superior-inferior (SI) oriented readout, interleaved every 25th TR. The SI-oriented readout was used as a projection-based navigator to identify and correct for respiratory motion, later in the reconstruction chain.

Phantom image acquisition

A resolution phantom was scanned on a 3T MAGNETOM Skyra using an 18-channel chest coil array and a 32-channel spine coil array (Siemens Healthcare, Erlangen, Germany) with the uppermost 12 elements activated, resulting in a total of 30 active receiver coils. The images were acquired with both the novel 3D-SWIG readout ordering as previously described in the

theory section, and a conventional 3D golden-angle readout ordering (15). The relevant imaging parameters for both sequences were: TE/TR = 1.7/3.4 ms, flip angle 50°, acquired isotropic voxel size 1.2 mm³, receiver bandwidth 1028 Hz/px. The sequence was triggered using a simulated ECG trace with an RR-interval of 1000 ms. The acquisitions were performed with 12, 48 and 192 simulated heart beats, excluding one dummy heat beat, and an equal number of sectors in the 3D-SWIG measurement.

Phantom image reconstruction

The raw data was exported from the scanner and imported into MATLAB 2019b (MathWorks, Natick, MA). The SI-projections were discarded prior to image reconstruction, and the motion correction step was skipped entirely for the phantom images. Images comprising all acquired data excluding the SI-projections were reconstructed by direct gridding using the gpuNUFFT toolbox (19), and the separate coil images were combined using a sum of squares approach. The ECG binning was performed based on the artificial ECG trace simulated on the scanner. A total of 20 equidistant time frames with a temporal width of 140 ms were reconstructed.

In-vivo image acquisition

Three subjects with clinical referral for CMR were asked to participate in the study. All subjects gave their written informed consent. The relevant imaging parameters were the same as the phantom acquisitions. The subjects were not given any additional instructions regarding their breathing other than what was communicated as part of their standard of care clinical CMR. The study was approved by the local ethics committee.

Motion correction and binning

The raw data were exported from the scanner and imported into MATLAB 2019b (MathWorks, Natick, MA). The SI-projections were extracted and a Fourier transform was applied along the readout direction. The first projection was selected as a reference, and the cross correlation was calculated between the reference projection and each of the subsequent projections to yield a correlation curve for each receiver coil. The coil that best represented the respiratory motion was then selected by analyzing the frequency spectrum of the cross-correlation signal. The coil that contained the highest frequency peak in the range 0.1–0.7 Hz was chosen to represent the respiratory motion. The selected motion signal was then interpolated to full temporal resolution using a smoothing spline interpolation. Rigid motion correction was performed by shifting each k-space line by applying a phase ramp with slope k, defined as

$$k \;=\; \frac{2\pi}{N}\, \Delta d \, cos(\theta) \tag{6}$$

where N was the number of sample points along each spoke, Δd was the estimated shift from the motion signal, and θ was the polar angle of the readout. The ECG data were extracted from the raw data file and each of the cardiac cycles was linearly stretched to a common temporal axis. A total of 20 image frames with a temporal width of 140 ms were reconstructed. See Figure 2 for a schematic overview of the motion correction and reconstruction process.

In-vivo image reconstruction

The *in vivo* datasets were reconstructed using the freely available image reconstruction software toolbox Berkley Advanced Reconstruction Toolbox (BART) (20). Singular value decomposition (SVD) based coil compression was used to reduce the number of receiver channels based on a cutoff defined as 5% of the maximum singular value. The number of receiver coils typically decreased from 30 to 15. Density compensation weights were

approximated as a uniform quadratic function. No tapering at high spatial resolutions nor k-space filters were used to artificially increase SNR. The coil sensitivity maps were calculated using an adaptive method (21) which was modified to calculate the coil sensitivity in a 3D volume as opposed to multiple 2D slices. A block size of 8x8x8 voxels was used. The phase of the images was set relative to the receiver coil with the highest magnitude. All images were reconstructed using both a simple gridding reconstruction and a compressed sensing algorithm, which can be described as solving the following minimization problem

$$\widehat{x} = \arg\min_{x} \lVert y - Ex \rVert_2^2 + \lambda_{xyz} \lVert \psi \, x \rVert_1 + \lambda_t \lVert \omega \, x \rVert_1 \qquad (7)$$

where x is the image, y is the measured k-space data, E is the encoding matrix which includes the coil sensitivity information, gridding operation and Fourier transform, λ_{xyz} is a spatial regularization parameter and λ_t is a temporal regularization parameter. The parameters λ_{xyz} and λ_t were selected based on prior experience. The operator ψ denotes the spatial sparsity transform, in this case spatial wavelets and ω denotes the temporal sparsity transform, in this case temporal total variation. The problem was solved using the alternating direction method of multipliers (ADMM) solver integrated in the BART toolbox.

Sampling uniformity

To estimate the sampling uniformity, spherical Voronoi tessellation of the surface of the sampling trajectory sphere after binning for all of the three patient acquisitions were calculated, resulting in a total of 60 binned k-spaces. The standard deviation of the Voronoi cell solid angle on the surface of the binned trajectory sphere was used as a metric of uniformity and the the uniformity was reported as mean ± SD in steradians (sr).

Point spread function analysis

The aliasing contribution to a voxel j from a unit-intensity voxel i can be obtained as

$$PSF(i, j) = e_j^* F^* F e_i \qquad (8)$$

where e_i was a zero vector with a single unitary value at the ith position and F^* and F were the adjoint and forward gridding operators respectively (22). The point spread function (PSF) was calculated for 12 patches, 48 patches and 192 sectors. In each case, 300 spokes were used per sector, resulting in a total of 3600, 14400 and 57600 spokes. The aliasing energy was calculated by resampling the PSF onto concentric radial shells and calculating the sum of the squared intensity of each shell as a function of the radial distance in k-space. This was used to classify the PSF of 3D-SWIG and conventional golden-angle for each of the spoke configurations. The radial Nyquist criterion for a 3D radial k-space can be calculated using the formalism from (23) as

$$P = M^2 \left(\frac{\pi}{2}\right) \qquad (9)$$

where P is the number of radial spokes needed to fulfill the Nyquist criterion in all parts of k-space, and M is the reconstructed matrix size. The undersampling factor was calculated for all spoke configurations.

Statistics

Continuous variables were presented as mean ± SD or median [interquartile range] as appropriate, and compared using the Wilcoxon signed rank test or Student's t-test. Normal distributions were determined using the Kolmogorov-Smirnov test. Durations of time were reported as mean time in minutes, rounded to the nearest integer. Statistical analysis was conducted using R (24).

Results

Time expenditure

After an initial survey with a single slice in 3 planes, an average of 4 minutes were spent acquiring additional survey scans and planning-projections such as vertical long axis (VLA) and pseudo short axis, followed by an average of 5 minutes spent on planning the anatomical planes, i.e. 2-chamber, 3-chamber, 4-chamber and short axis. The cine images were acquired in 3 minutes, including breath hold-commands and a 3 second recovery period between each breath hold. In total, an average of 12 minutes was spent acquiring survey scans and cine images. Assuming a heart rate of 60 BPM, the 3D-SWIG acquisition takes 12 seconds, 48 seconds and 3 minutes 12 seconds for 12, 48 and 96 patches, respectively. An experienced observer was able to find the same anatomical projections (2-chamber, 3-chamber, 4-chamber and short axis) retrospectively from the 3D-SWIG whole-heart volume in an average of 2 minutes. A summary of the time expenditure is available in Table 1.

Sampling uniformity

Simulated results of k-space binning using an artificial ECG trace are shown in Figure 3. The 3D-SWIG sampling points' distribution is visibly more uniform than the golden-angle sampling points and this is corroborated by the numerical value calculate for each Voronoi diagram. In the clinical population, the standard deviation of Voronoi cell areas was found to be larger ($p < 0.0001$) for golden-angle, $1.17 \pm 0.141 \times 10^{-3}$ sr than for SWIG, $0.683 \pm 0.0958 \times 10^{-3}$ sr, see Figure 4.

PSF Analysis

Quantitative and qualitative analysis of the PSF are presented in Figure 5. At high undersampling factors (12 beats, 3600 spokes, R = 16) there is a considerable difference

between the shapes of the curves. The streak-free-region, where the aliasing energy is close to zero extends further out, corresponding to higher spatial resolutions, for the 3D-SWIG profile ordering compared to conventional golden-angles. As the undersampling decreases, (48 beats, 14,400 spokes, R = 4) the aliasing energy curves appear to converge. Finally, at full sampling (192 beats, 57600 spokes, R = 1) the curves are virtually indistinguishable. The PSF images corroborate the numerical findings, but reveal a smoother appearance for 3D-SWIG for all undersampling factors.

Phantom image analysis

Phantom images reconstructed from all available spokes are presented in Figure 6. Simulated binning images, using the on-scanner simulated ECG trace are displayed in Figure 7. There is visibly less streaking obscuring the underlying object, corroborating the findings from the numerical PSF analysis. Even at extremely high undersampling factors (R=52.3) the overall structure of the phantom is well preserved for 3D-SWIG. However, the conventional golden-angle profile ordering shows severe aliasing artifacts obscuring the phantom.

In vivo image analysis

Representative examples from the *in vivo* acquisitions are presented in Figure 8. The images are acquired in 48 heartbeats/sectors and are displayed as a straight transversal slice through the thorax. The left column shows the images reconstructed using direct gridding, and despite heavy streaking in both acquisitions, in 3D-SWIG the underlying structure of the heart can still be seen. The right column shows the same acquisitions, reconstructed with a compressed sensing algorithm using identical parameters for both conventional golden-angle and 3D SWIG. It is apparent that the conventional golden-angle image reconstruction was unable to converge to an acceptable solution, where the 3D-SWIG reconstruction results in images with little

blurring and minor residual streaking outside of the body. Multiplanar reformatted versions of the same two acquisitions are shown in Figure 9. Here, all images are reconstructed using the compressed sensing algorithm. The top row shows conventional golden-angle images where the compressed sensing algorithm was unable to reconstruct a clinically usable image, and the bottom row show the corresponding image reconstructions from the 3D-SWIG acquisition, displaying excellent image quality. The reformatted images have been merged in to a reconstructed slice thickness of 7.2 mm to mimic what is conventionally used in 2D CMR. In order to visualization the temporal fidelity over the cardiac cycle, a so-called M-mode image is displayed in Figure 9B.

Discussion

In this work, we have proposed 3D-SWIG, a novel golden-angle-based profile ordering based on acquiring the three-dimensional k-space in sectors or patches on the trajectory sphere. We have demonstrated superior performance compared to the conventional double golden-angle method, due to improved k-space uniformity after physiological binning.

The main finding of this study is that the 3D-SWIG profile ordering is able to acquire clinically acceptable whole-heart cine images under free breathing in less than one minute. The total time to obtain the standard anatomical projections was compared to a conventional 2D workflow by an experienced radiographer, and our results show that 3D-SWIG is able to reduce the time expenditure of the imaging process by half, or less.

By convention, $\phi_1 = 0.4656$ and $\phi_2 = 0.6823$ have been used for 3D golden-angle based imaging. These numbers are based on the so called super-golden ratio, or the fourth smallest of the Pisot numbers. There are other values for ϕ with similar properties to the super-golden ratio,

such as the plastic ratio, which is the smallest of the Pisot numbers. However, the benefit of using other ratios remains to be explored. A desirable property that is common for all golden-angle techniques is that the angles are generated by an *open* low-discrepancy set, i.e. that the angles distribute themselves evenly, without ever repeating. When limited to one heart-beat per patch, this condition could be relaxed, as there is a limited number of points that can be distributed within that patch. Previous work has demonstrated that it's possible to obtain a more even distribution using a closed set, as long as the period of repetition is longer than the actual acquisition. An example of this is the pseudo-golden-angles. The golden-angle is the limit of ratios of successive Fibonacci numbers, but by truncating the limit, a closed set is obtained that have lower discrepancy than the conventional golden-angles (25).

There are some important limitations of the current work that need to be considered. First and foremost that the reconstructed temporal window was 140 ms, which was chosen to match previous work using free running whole-heart imaging (8). It's important to note that this number is higher than what is conventionally used in 2D breath held imaging, and future investigations are needed to determine how this would affect the clinical utility of the approach. It would be possible to increase the temporal resolution, likely at the expense of more streaking artifacts. Likewise, it remains to be investigated how the image quality would be affected by reconstructing images with a smaller temporal footprint. The approach was tested in a limited cohort with only 3 subjects, and systematic testing in a larger cohort and with more quantitative evaluations is warranted. The optimal acquisition time remains to be determined, and how this may vary depending on the clinical question at hand. Furthermore, the image reconstruction was performed with a compressed sensing algorithm, with regularization over the temporal dimension. The degree of temporal regularization has to be selected manually. In this study, the same regularization parameters were used for both acquisition strategies and all acquisitions. It

can be argued that the parameter should be optimized for each acquisition, or each acquisition strategy and the benefit of this remains to be evaluated. The regularization parameter was selected based on prior experience, but the effect of using a lower degree of temporal regularization was not investigated. However, from Figure 9B, it appears as if the temporal fidelity is well preserved and there is apparent temporal smoothing of the cardiac cycle.

Future work may include five-dimensional (5D) imaging (11), where the respiratory motion is handled by reconstructing multiple respiratory phases, as opposed to performing motion correction as in the current work. Another interesting use is fetal CMR, where the self-gating capabilities and lack of fold-over artifacts could be especially useful.

Conclusion

In conclusion, a novel free-running 3D sector-wise golden-angle radial (3D-SWIG) profile ordering is proposed. It provides better k-space uniformity than the conventional double golden-angle profile ordering and can achieve isotropic whole-heart coverage in less than one minute of free-breathing acquisition. The feasibility of this approach has been demonstrated through numerical simulations, phantom acquisitions and in 3 patients.

Acknowledgements

References

1. Lu X, Jolly MP, Georgescu B, et al. Automatic view planning for cardiac MRI acquisition. In: Fichtinger G, Martel A, Peters T, editors. Medical Image Computing and Computer-Assisted Intervention -- MICCAI 2011. Berlin, Heidelberg: Springer Berlin Heidelberg; 2011. pp. 479–486.

2. Nitta S, Takeguchi T, Matsumoto N, Kuhara S, Yokoyama K, Ishimura R, Nitatori T. Automatic slice alignment method for cardiac magnetic resonance imaging. Magn. Reson. Mater. Physics, Biol. Med. 2013;26:451–461.

3. Jagsi R, Moran JM, Kessler ML, Marsh RB, Balter JM, Pierce LJ. Respiratory Motion of The Heart and Positional Reproducibility Under Active Breathing Control. Int. J. Radiat. Oncol. Biol. Phys. 2007;68:253–258.

4. Pipe JG. Motion correction with PROPELLER MRI: Application to head motion and free-breathing cardiac imaging. Magn. Reson. Med. 1999;42:963–969.

5. Larson AC, Kellman P, Arai A, Hirsch GA, McVeigh E, Li D, Simonetti OP. Preliminary investigation of respiratory self-gating for free-breathing segmented cine MRI. Magn. Reson. Med. 2005;53:159–168.

6. Kellman P, Chefd'hotel C, Lorenz CH, Mancini C, Arai AE, McVeigh ER. High spatial and temporal resolution cardiac cine MRI from retrospective reconstruction of data acquired in real time using motion correction and resorting. Magn. Reson. Med. 2009;62:1557–1564.

7. Stehning C, Börnert P, Nehrke K, Eggers H, Stuber M. Free-breathing whole-heart coronary MRA with 3D radial SSFP and self-navigated image reconstruction. Magn. Reson. Med. 2005;54:476–480.

8. Coppo S, Piccini D, Bonanno G, Chaptinel J, Vincenti G, Feliciano H, Van Heeswijk RB, Schwitter J, Stuber M. Free-running 4D whole-heart self-navigated golden angle MRI: Initial results. Magn. Reson. Med. 2015;74:1306–1316.

9. Sigfridsson A, Kvitting JPE, Knutsson H, Wigström L. Five-dimensional MRI incorporating simultaneous resolution of cardiac and respiratory phases for volumetric imaging. J. Magn. Reson. Imaging 2007;25:113–121.

10. Holst K, Ugander M, Sigfridsson A. Respiratory Resolved Cardiac Cine Imaging using Self-Gated Golden Angle Radial Acquisition. In: proc. ISMRM. ; 2015.

11. Feng L, Coppo S, Piccini D, Yerly J, Lim RP, Masci PG, Stuber M, Sodickson DK, Otazo R. 5D whole-heart sparse MRI. Magn. Reson. Med. 2017;00:1–13.

12. Han F, Zhou Z, Rapacchi S, Nguyen KL, Finn JP, Hu P. Segmented golden ratio radial reordering with variable temporal resolution for dynamic cardiac MRI. Magn. Reson. Med. 2016;76:94–103.

13. Fyrdahl A, Ramos JG, Eriksson MJ, Caidahl K, Ugander M, Sigfridsson A. Sector-wise golden-angle phase contrast with high temporal resolution for evaluation of left ventricular diastolic dysfunction. Magn. Reson. Med. 2020;83:1310–1321.

14. Pang J, Sharif B, Fan Z, Bi X, Arsanjani R, Berman DS, Li D. ECG and navigator-free four-dimensional whole-heart coronary MRA for simultaneous visualization of cardiac anatomy and function. Magn. Reson. Med. 2014;72:1208–1217.

15. Chan RW, Ramsay EA, Cunningham CH, Plewes DB. Temporal stability of adaptive 3D radial MRI using multidimensional golden means. Magn. Reson. Med. 2009;61:354–363.

16. Anderson PG. Multidimensional Golden Means. Appl. Fibonacci Numbers 1993;5:1–9.

17. Niederreiter H. Point sets and sequences with small discrepancy. Monatshefte für Math. 1987;104:273–337.

18. Roşca D, Plonka G. Uniform spherical grids via equal area projection from the cube to the sphere. J. Comput. Appl. Math. 2011;236:1033–1041.

19. Knoll F, Schwarzl A, Diwoky C, Sodickson DK. gpuNUFFT - An open source GPU library for 3D regridding with direct Matlab interface. In: Proceedings 22. Annual Meeting

International Society for Magnetic Resonance in Medicine. Vol. 22. Milan, Italy; 2014. p. 4297.

20. Uecker M, Tamir JI, Bahri D, Virtue P, Cheng J, Zhang T, Lustig M. Berkeley advanced reconstruction toolbox. In: Proceedings of the 23rd annual meeting of ISMRM. Toronto. ; 2015. p. 2486.

21. Walsh DO, Gmitro AF, Marcellin MW. Adaptive reconstruction of phased array MR imagery. Magn. Reson. Med. 2000;43:682–690.

22. Lustig M, Donoho DL, Pauly JM. Sparse MRI: The application of compressed sensing for rapid MR imaging. Magn. Reson. Med. 2007;58:1182–1195.

23. Winkelmann S, Schaeffter T, Koehler T, Eggers H, Doessel O. An optimal radial profile order based on the golden ratio for time-resolved MRI. IEEE Trans. Med. Imaging 2007;26:68–76.

24. R Core Team. R: A Language and Environment for Statistical Computing. 2017.

25. Svedin BT, Payne A, Bolster BD, Parker DL. Multiecho pseudo-golden angle stack of stars thermometry with high spatial and temporal resolution using k-space weighted image contrast. Magn. Reson. Med. 2018;79:1407–1419.

Tables

Table 1. Summary of the time spent on each task necessary to plan and acquire all standard image projections using a conventional breath-held 2D workflow compared to the 3D-SWIG acquisition.

	2D workflow	3D-SWIG (48 sectors)	3D-SWIG (192 sectors)
Pseudo-projections	4 min	–	–
Planning	5 min	–	–
Acquisition	3 min	1 min	4 min
Multiplanar reformatting	–	2 min	2 min
Total	**12 min**	**3 min**	**6 min**

Figure captions

A

B

12 PATCHES   **48 PATCHES**   **192 PATCHES**
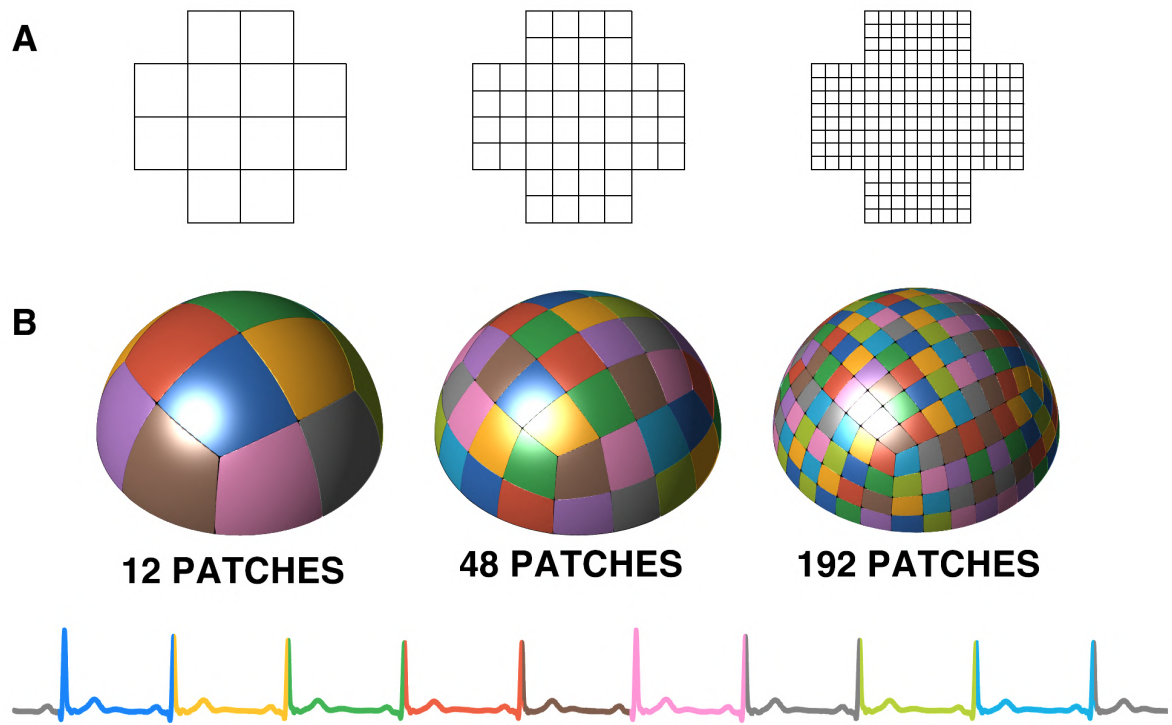
Figure 1. A: The unfolded half-cube illustrates the tiling. Each tile in the grid is filled according to the double golden-angle within the tile and subsequently mapped to the hemisphere. B: Illustrative examples of the grid mapped onto the hemisphere. B) Color coded patches and RR-intervals illustrates that each patch is acquired during a single heartbeat.
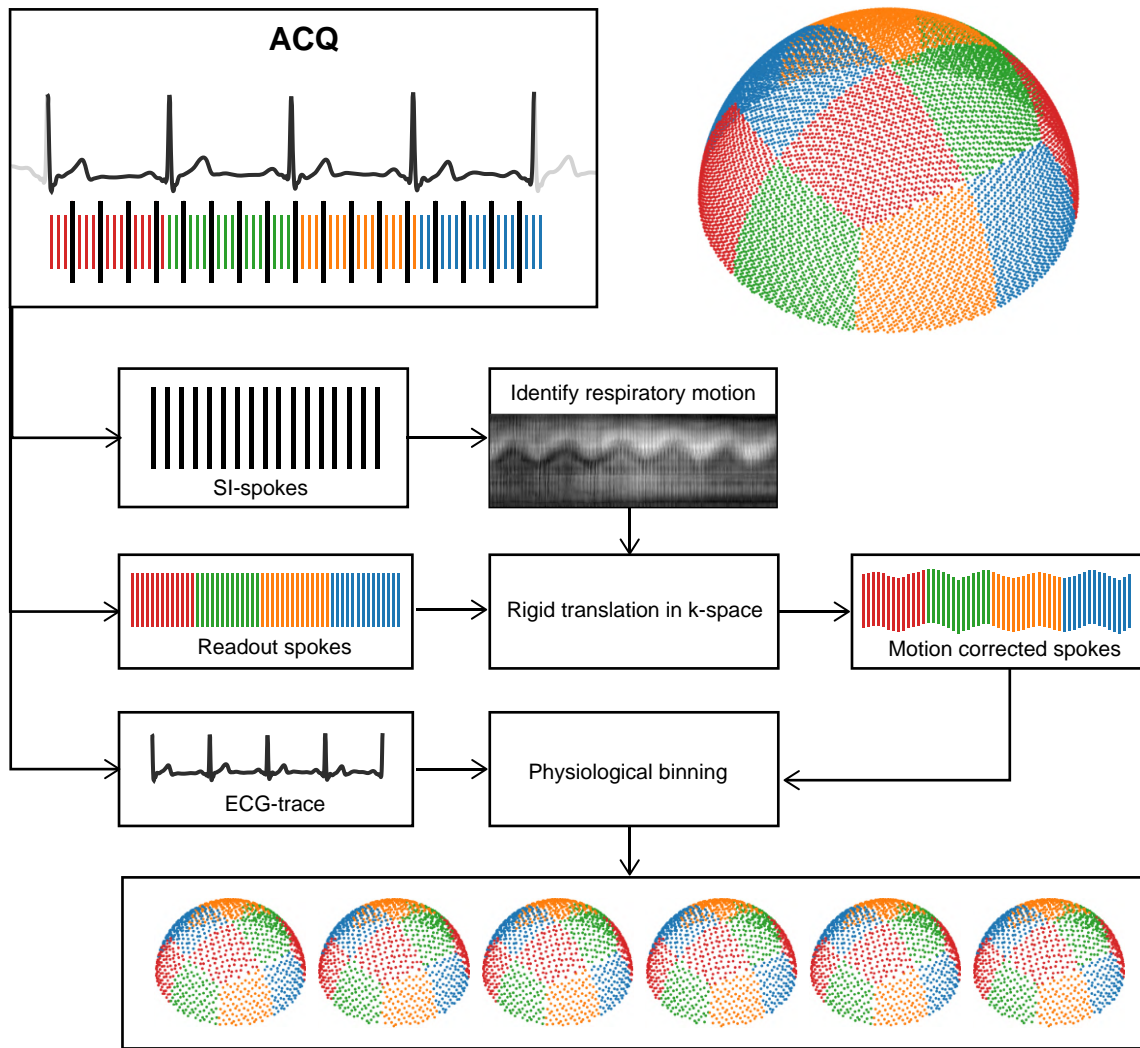
Figure 2. A schematic flow-chart describing the acquisition process. Superior-inferior (SI) projection spokes are interleaved into the readout, and can be used to identify respiratory motion. This motion is then extracted by means of normalized cross correlation, yielding a spatial shift. Each readout line is then shifted by the appropriate amount by applying a phase ramp in the frequency domain. Using the recorded ECG trace, the k-space is then divided into bins corresponding to different parts of the cardiac cycle. Notably, each patch/tile is sampled in a single heart cycle, resulting in improved uniformity compared to conventional golden-angle binning.

SIMULATED BINNING

| 12 BEATS	48 BEATS	192 BEATS
R = 52.3 (492 spokes)	R = 13.1 (1968 spokes)	R = 3.7 (6912 spokes)
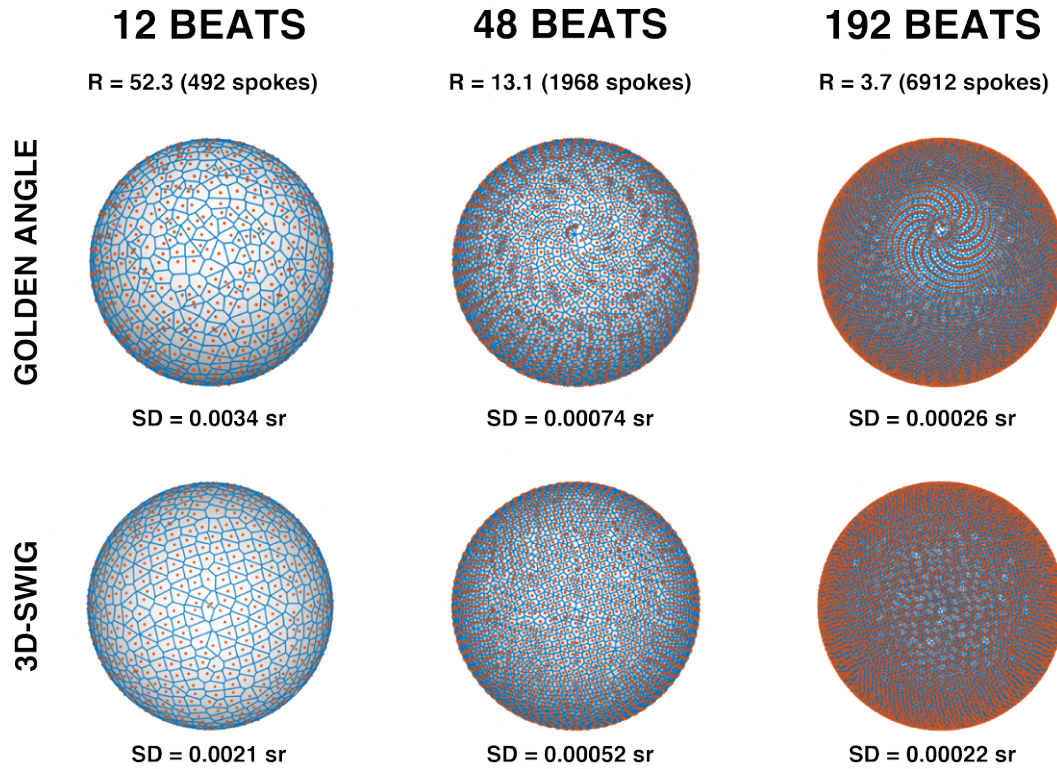
Figure 3. Spherical Voronoi diagrams give both a qualitative and quantitative indicator of the higher level of uniformity from the 3D-SWIG method over the conventional golden-angle method after binning. The standard deviation below each Voronoi diagram refers to the standard deviation of the solid angle in steradians for the Voronoi cell in the diagram.
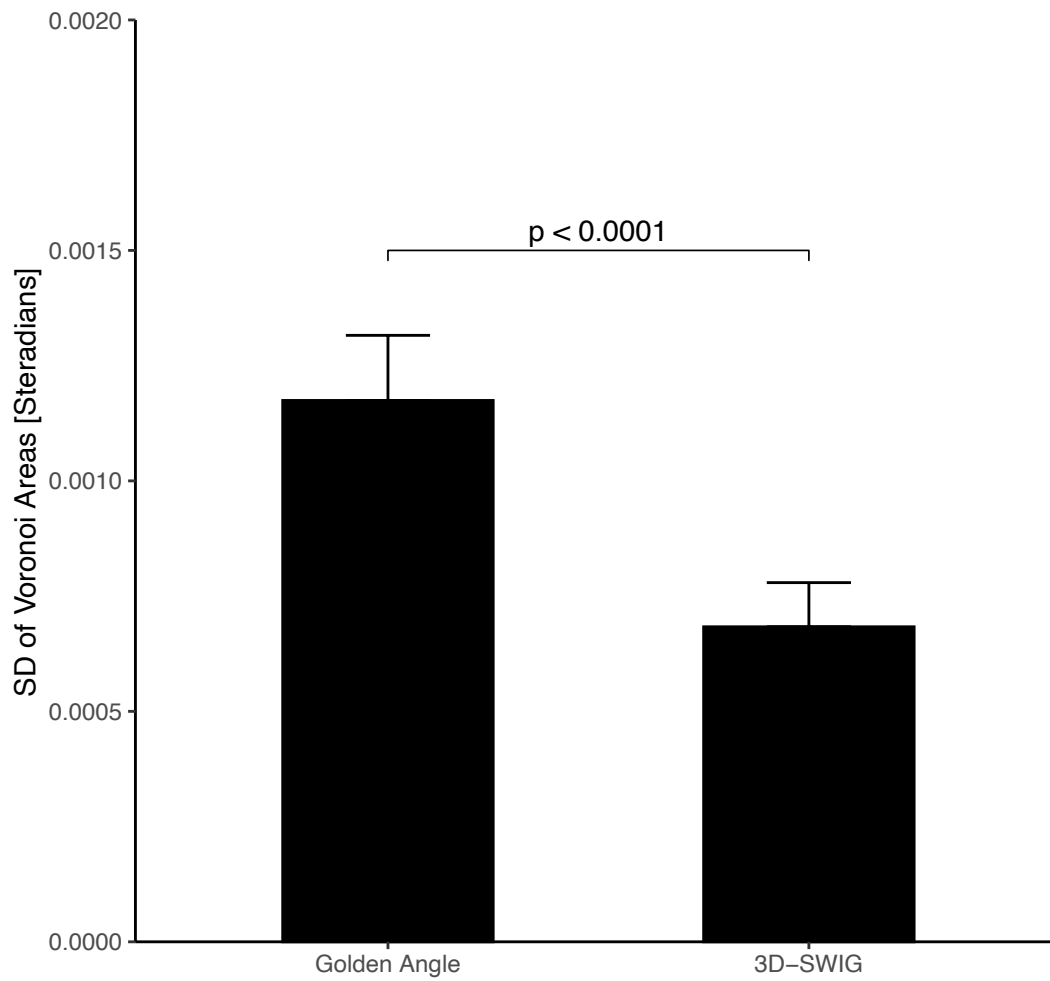
Figure 4. The k-space uniformity assessed by the standard deviation of Voronoi cell sizes on the trajectory sphere surface for each calculated k-space bin. The standard deviation was calculated for 20 bins in 3 patients, using real ECG-data. The lower values for 3D-SWIG indicate a greater uniformity of k-space sampling. Error bars denote one standard deviation of the uniformity measure.
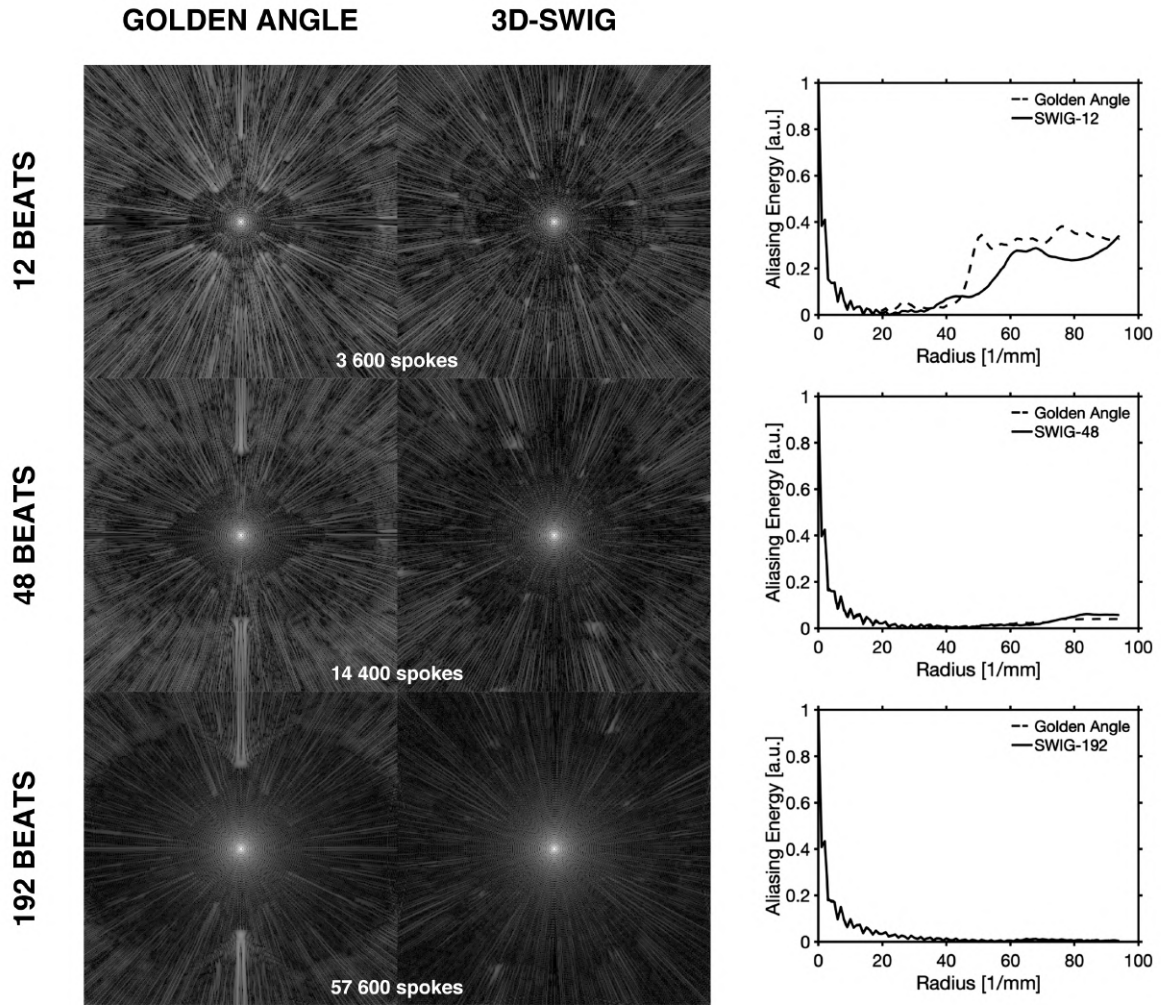
Figure 5. Point spread functions (PSF) for golden-angle and 3D-SWIG with 12, 48 and 192 heartbeats or patches. The PSFs are displayed on a logarithmic scale. The right column shows numerically the sum of PSF values as a function of PSF radius. A lower aliasing energy is better. These plots suggest that 3D-SWIG acquisitions exhibit less streaking artifacts for high undersampling, but as the number of spokes increases, the difference between golden-angle and 3D-SWIG decreases.
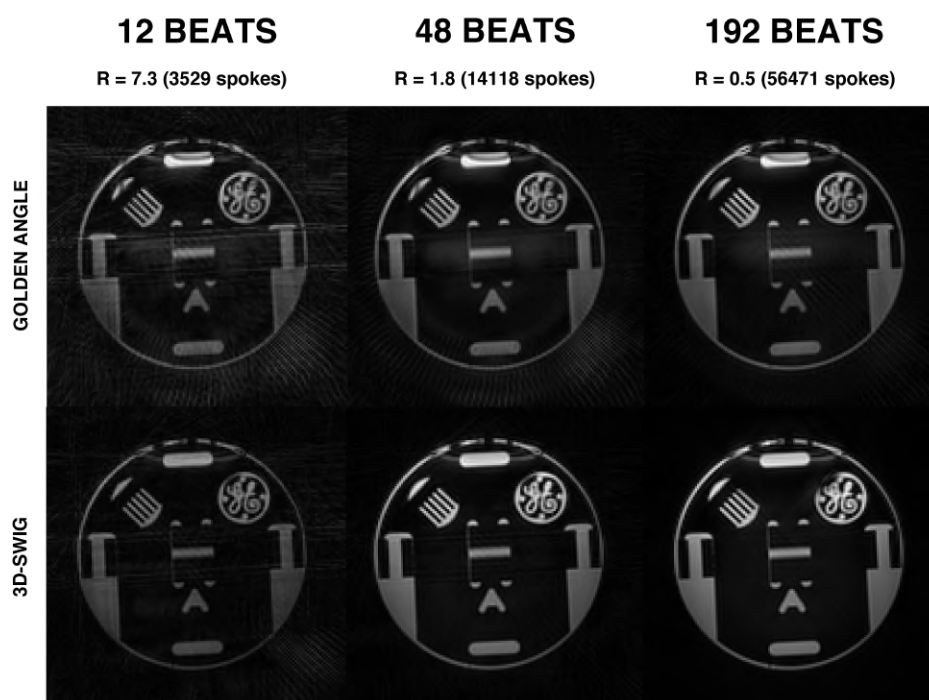
Figure 6. Phantom images reconstructed from all available spokes. The number of heartbeats corresponds to the number of sectors in the 3D-SWIG profile ordering. The reported undersampling factor is relative to the Nyquist criterion for a spherical k-space and a matrix size of 128x128x128 isotropic.
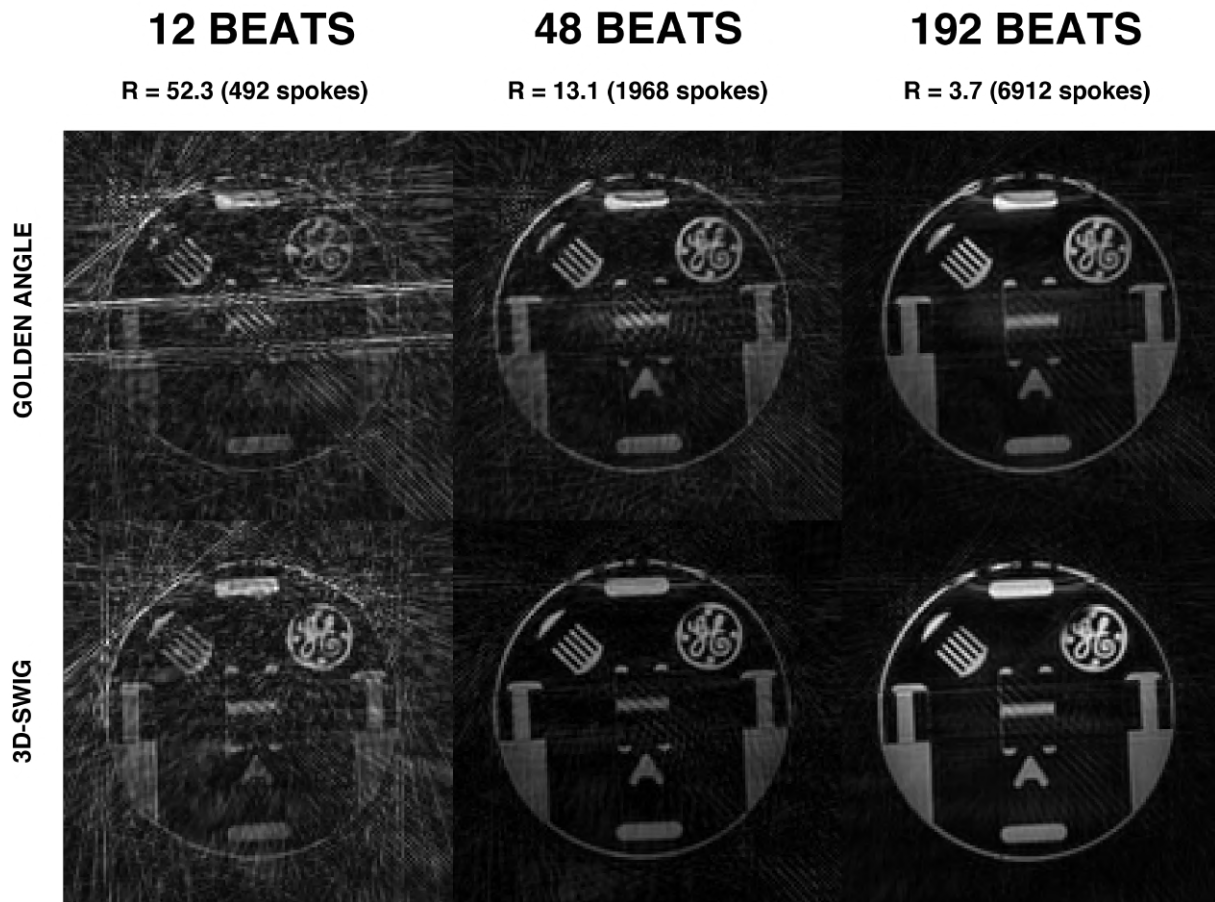
Figure 7. Phantom images reconstructed using binned data. Binning was simulated with a reconstructed window width of 140ms using the simulated ECG. The reported undersampling factor is relative to the Nyquist criterion for a spherical k-space and a matrix size of 128x128x128 pixels.
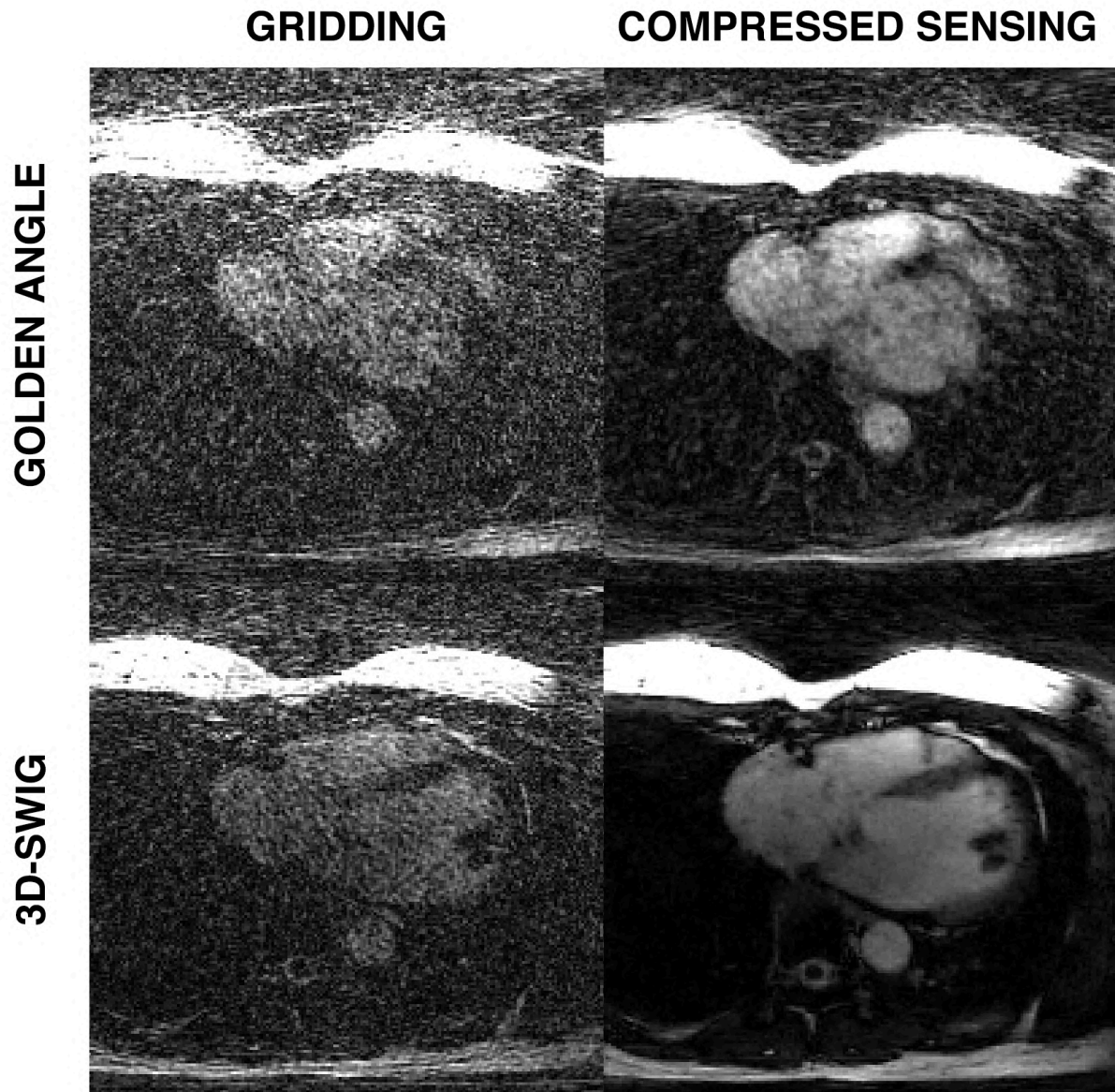
Figure 8. Representative examples of two acquisitions from one subject acquired in 48 heartbeats each during free breathing, illustrating axial images from the conventional golden-angle profile ordering and the 3D-SWIG profile ordering, with and without the compressed sensing reconstruction. Both the acquired and reconstructed voxel size is 1.2 mm isotropic. All images are reconstructed in the BART toolbox. All reconstruction parameters are equal between the two cases. The cardiac cycle is binned into 20 cardiac phases with a temporal window of 140 ms, the same window width used in the phantom experiments.
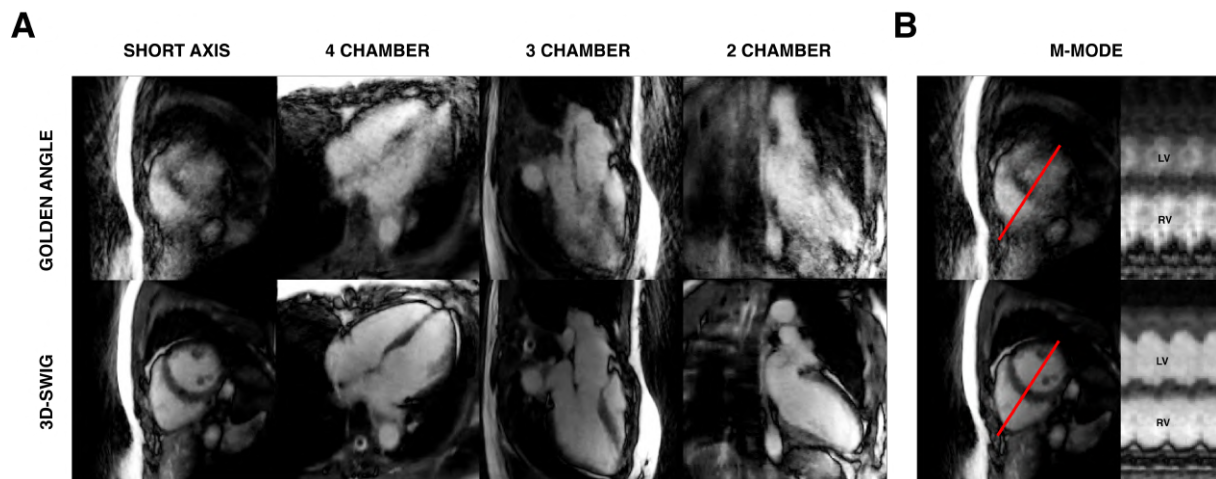
Figure 9. A: Illustrative examples of multiplanar reformatted images in the standard anatomical projections. A total of 6 slices (slice thickness 1.2mm) have been merged together to create a reconstructed slice thickness of 7.2 mm which is similar to what is conventionally used in 2D-cine CMR. The cardiac cycle is binned into 20 cardiac phases with a temporal window of 140 ms. The acquisition time for both methods was 48 heart beats. The images represent the end-diastolic cardiac phase.

B: The cardiac cycle is displayed in a so-called motion mode (M-mode) image where a single line, indicated in red, is displayed over time. The right ventricle is indicated as "RV" and the left ventricle as "LV".